


Article

Study on the Tensile Failure Characteristics and Energy Calculation Model of Coal Seam Hard Roof Considering the Mining Speed

Wenlong Li ¹, Shihao Tu ^{2,*}  and Tongbin Zhao ¹

¹ College of Energy and Mining Engineering, Shandong University of Science and Technology, Qingdao 266590, China; 18361260569@163.com (W.L.); ztbwh2001@163.com (T.Z.)

² State Key Laboratory of Coal Resources and Safe Mining, School of Mines, China University of Mining and Technology, Xuzhou 221116, China

* Correspondence: tsh@cumt.edu.cn

Abstract: To reveal the influence mechanism of mining speed on roof fracture-type rockburst, the Brazilian split technique combined with acoustic emission monitoring technology was employed to study the effects of loading rates on the tensile failure characteristics and acoustic emission parameters of coal series sandstone. The linear relationship between the tensile strength of the samples and the change rate of tensile stress was determined. The mining speed was introduced into the mechanical model of initial and cyclic fracture of the hard roof, and the quantitative relationship between the maximum rate of change of tensile stress within the hard roof and the mining speed was derived. Based on this, a computational model for the bending elastic energy of the hard roof during initial and cyclic fractures, considering the mining speed, was established. The main findings are as follows: As the loading rate increases, the distribution range of acoustic emission energy in sandstone Brazilian split samples before failure widens, with a significant rise in acoustic emission ring-down counts and energy at failure. At lower loading rates, acoustic emission events primarily occur near sample failure, whereas at higher rates, they mostly happen in the early loading stage. The higher the mining speed, the less opportunity there is for internal micro-fractures to develop and expand before the hard roof fractures, which macroscopically results in increased tensile strength and a larger amount of energy released at the moment of fracture. Bending elastic energy rises approximately linearly with mining speed, and the thicker the hard roof, the more sensitive the bending elastic energy is to changes in mining speed. This effect is even more pronounced during cyclic fractures. Optimizing mining speed is crucial for preventing roof fracture-type rockbursts, especially in mining workfaces with thick and hard roofs.

Keywords: hard roof; Brazilian splitting test; tensile strength; bending elastic energy; mining speed



Citation: Li, W.; Tu, S.; Zhao, T. Study on the Tensile Failure Characteristics and Energy Calculation Model of Coal Seam Hard Roof Considering the Mining Speed. *Appl. Sci.* **2024**, *14*, 5734. <https://doi.org/10.3390/app14135734>

Academic Editor: Andrea L. Rizzo

Received: 9 April 2024

Revised: 26 June 2024

Accepted: 26 June 2024

Published: 1 July 2024



Copyright: © 2024 by the authors. Licensee MDPI, Basel, Switzerland. This article is an open access article distributed under the terms and conditions of the Creative Commons Attribution (CC BY) license (<https://creativecommons.org/licenses/by/4.0/>).

1. Introduction

The occurrence of rockbursts in coal mines is significantly influenced by the behavior of hard roofs [1], where tensile failure, along with the dynamics of energy accumulation and release, plays a crucial role. An understanding of the interplay of mechanical failure and energy dynamics is essential for comprehending rockburst mechanisms. Additionally, the mining speed significantly affects the fracture characteristics of hard roofs, mainly because of the fact that it induces the variations in the loading rate of the overlying rock load on the roof [2]. This means that in order to reveal the mechanisms as mentioned above and to understand how they are affected by the mining speed, it is necessary to analyze the tensile failure characteristics and establish an energy model for hard roofs subjecting them to the influence of varied mining speeds.

Currently, research on the effects of loading rates on the tensile failure characteristics of rock bodies primarily relies on experimental analysis, with direct tension and Brazilian

split tests being the main experimental methods. For example, Wu [3] found through experimental research that the tensile strength of granite significantly increases with an increase in the loading rate. Li et al. [4] conducted direct tensile tests on gypsum and granite under different strain rate conditions and concluded that tensile strength significantly increases with the loading rate, consistent with the results of the Brazilian split tests. Zhou et al. [5] carried out uniaxial tensile strength tests on hard and brittle marble at different loading rates, finding that the peak tensile strength of the rock samples increases logarithmically with the loading rate. Gong et al. [6] conducted Brazilian split tests on sandstone under different loading rates within the quasi-static and dynamic strain rate range, and based on the test results, established an empirical equation describing the strain rate effect on the tensile strength of sandstone. Yang et al. [7] understood the rule that the tensile strength of sandstone increases with the loading rate through Brazilian split experiments and explained the mechanism by which the loading rate affects the tensile strength using elastic dynamics methods and the principles of molecular scale functions. Deng et al. [8], taking surface sandstone as the research object, conducted split tests under different loading rates within the quasi-static strain rate range, and found that the tensile strength increases rapidly at first and then more slowly with the loading rate, and by analyzing the energy parameters and changes in the morphology of the split surface, revealed the impact mechanism of loading rate on tensile strength. Cui et al. [9] studied Brazilian split tests of granite, basalt, and limestone under different loading rates, analyzing the impact of the loading rate on the morphology of the split surface based on optical 3D scanning technology. Liu et al. [10] conducted direct tensile tests on granite under different loading rates, showing that both tensile strength and the roughness of the split surface increase with the loading rate. Liu et al. [11] performed Brazilian split tests on coal samples under different loading rates, analyzing the impact of the loading rate on the acoustic emission parameters, infrared radiation, deformation field, and energy evolution. Vasylijev et al. [12] improved an analytical technique to calculate the strength of cylindrical rock samples taking into consideration standard horizontal stresses. Winkler et al. [13] investigated the influence of different transversely isotropic parameters and their ratios on the elastic behavior of cylindrical rock samples in uniaxial compression tests. Piscopo et al. [14] developed new design formulas for the ultimate strength of platings under uniaxial compression, with short and/or long edges elastically restrained against torsion. Choo et al. [15] investigated size effects on the compressive strength and cracking behavior of flawed rocks through high-fidelity simulations of mixed-mode fracture in quasi-brittle materials. Tomporowski et al. [16] obtained the modelling of fractures in pre-flawed marble specimens during uniaxial compression by Application of the 3D DEM.

Research on the influence of mining speed on the energy accumulation in hard roofs primarily focuses on theoretical analysis. For instance, Feng et al. [17] derived an analytical expression for the bending elastic energy density by deducing certain things from the cantilever beam model of the hard roof, indirectly and qualitatively analyzing the impact of the main factors (cantilever length, peak stress concentration factor, peak stress distance from the coal wall) on bending elastic energy under the control of mining speed. Based on the relationship between the tensile strength of rock layers and loading rates, Zhao et al. [18] established a calculation method for finding the bending elastic energy of hard roofs that considers the effect of loading rates.

The research mentioned above has achieved certain results in understanding the effects of loading rates on the tensile strength of rock bodies and the influence of mining speed on energy accumulation in hard roofs. However, there are still some research gaps in the following areas: the impact of loading rates on the acoustic emission characteristic parameters of coal series sandstone, the relationship between mining speed and the rate of change in tensile stress within the hard roof, and the direct influence pattern of mining speed on the bending elastic energy of hard roofs. Therefore, this paper utilizes the Brazilian split test to explore the influence of loading rates on the tensile failure characteristics and acoustic emission parameters of coal series sandstone. Through theoretical deduction, the

relationship between mining speed and the rate of change in tensile stress within the hard roof was derived. A computational model for the bending elastic energy of the hard roof during initial and cyclic fractures, taking into account the mining speed, was established, and an analysis of the main influencing factors was conducted.

2. Methods

2.1. Experimental Purpose

A vast body of experimental research has demonstrated that the tensile strength of coal series sandstone is approximately linearly related to the loading rate [19–23]. However, due to the wide distribution of coal series sandstone and the significant variation in its mechanical properties, coupled with the diversity in loading methods and the range of loading rates, the coefficients in the linear relationship are difficult to directly determine. Therefore, it is necessary, considering the actual conditions of the research subject of this paper, to explore the tensile failure characteristics of hard sandstone roofs under different loading rates. This exploration work involves analyzing the mechanical response characteristics, spatiotemporal evolution characteristics of acoustic emission parameters, and pre-peak energy accumulation characteristics under different loading rates, to lay the experimental foundation for establishing an energy calculation model for hard roofs.

2.2. Experimental Design and Scheme

(1) Sample Acquisition

The experimental rock samples were obtained from the fine sandstone roof of the 23,908 working face of the No. 9 coal seam, Xi San Mountain mining area, Zhang Shuanglou Coal Mine, Pei County, Xuzhou City, Jiangsu Province. Based on the impact propensity identification results, the average uniaxial compressive strength is 51.84 MPa, and the average elastic modulus is 9.70 GPa, indicating a strong tendency for impact. In accordance with the Methods for Determining the Physical and Mechanical Properties of Coal and Rock Part 10: Methods for Determining the Tensile Strength of Coal and Rock (GB/T 23561.10-2010 [24]), the rock samples were processed into specimens with a diameter of 50 mm and thickness of 30 mm, as shown in Figure 1.

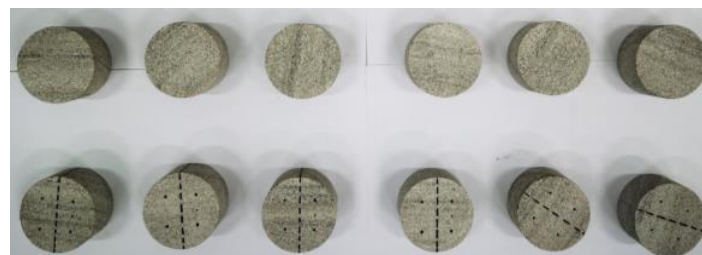


Figure 1. Brazil splitting test specimen.

(2) Experimental Scheme Design

Currently, the Brazilian split test is a widely applied method for rock tensile failure experiments [25]. This chapter uses the Brazilian split test to study the mechanical characteristics of hard roof sandstone under different loading rates. The experiment is conducted on an MTS C64.106 (Metus Industrial Systems Co., LTD, Shanghai, China) electro-hydraulic servo universal testing machine (see Figure 2), using a Brazilian split test mold to secure the specimen at the center of the testing machine's pressure plate. The loading is controlled by load, with loading rates set at 0.1, 0.5, 1.0, and 5.0 kN/s, for a total of four levels. Three sets of experiments are conducted for each loading rate level. To analyze the evolution of micro-cracks within the rock sample during the loading process, the Express-8 acoustic emission system is used to monitor the acoustic emission signals in real time during the experiment. The acoustic emission threshold is set to 40 dB, the peak identification time is

set to $PDT = 50 \mu s$, the hit identification time is set to $HDT = 200 \mu s$, and the hit lockout time is set to $HLT = 300 \mu s$. The signal collection frequency is set at 140 kHz, with four acoustic emission probes used, arranged as shown in Figure 3. Before the official start of the experiment, a coupling agent is applied between the probe and the sample to enhance signal transmission, and a lead break test is conducted to simulate the signal source, monitoring the signal reception of each channel to ensure that each probe can normally receive signals. Additionally, the acoustic emission system and the testing machine system are synchronized in timing to ensure that the data collected by the two systems are consistent in time. Then, the rock samples are loaded at different loading rates until they fracture, and the related data are stored.

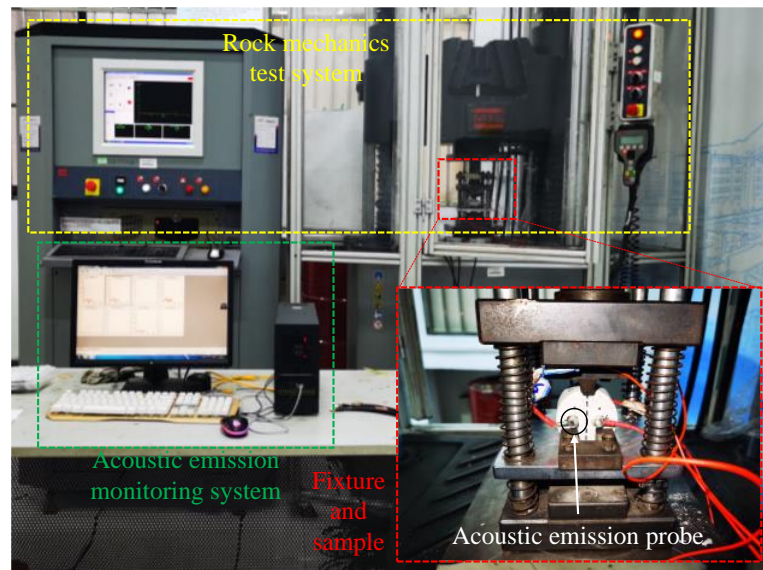


Figure 2. Test system.

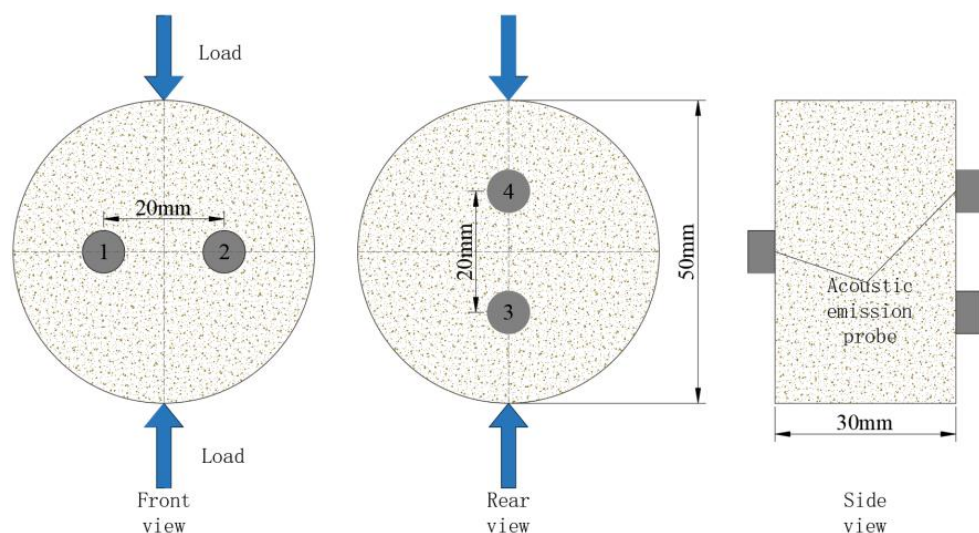


Figure 3. Arrangement of acoustic emission probes.

3. Results

3.1. Mechanical Response Characteristics

Under the action of radial load, the tensile stress (σ_x) at the center of the Brazilian split test sample is:

$$\sigma_x = -\frac{2P}{\pi DL} \quad (1)$$

where P is axial load, D is the diameter of the Brazilian splitting specimen, L is the thickness of the Brazilian splitting specimen.

To analyze the mechanical response characteristics of the samples under different loading rate conditions, the failure load of each group of samples was statistically analyzed. Using Equation (1), the loading rate was converted into the change rate of tensile stress at the center of the sample, and the failure load was converted into tensile strength. The results are shown in Table 1. In the following discussion, the median tensile strength of the results from each group will be used as the subject of analysis (corresponding sample numbers are sequentially 1-2, 2-1, 3-3, 4-3).

Table 1. Failure load and tensile strength of each group.

Sample Number	Loading Rate/ $\text{kN}\cdot\text{s}^{-1}$	Rate of Change of Tensile Stress/ $\text{MPa}\cdot\text{s}^{-1}$	Failure Load/ kN	Tensile Strength/ MPa	Median Tensile Strength/ MPa
1-1 1-2 1-3	0.1	0.04	16.04 18.05 18.84	6.81 7.66 8.00	7.66
2-1 2-2 2-3			18.24 19.17 16.25	7.75 8.14 6.90	
3-1 3-2 3-3			16.31 19.42 18.31	6.93 8.25 7.77	
4-1 4-2 4-3	5.0	2.12	19.23 16.22 18.62	8.17 6.89 7.91	7.91

The variation curve of tensile stress at the center of the sample under different loading rate conditions during the loading process is shown in Figure 4. It is observed that, before the peak failure point, the tensile stress at the center of the sample gradually increases with the increase in loading displacement. At the moment of specimen failure, the tensile stress measured at the center represents its tensile strength. The relationship between tensile strength and the change rate of tensile stress is illustrated in Figure 5. Through fitting analysis, they approximately exhibit a linear relationship, with a correlation coefficient reaching 0.89029 (>0.8), indicating a good fit of the regression model.

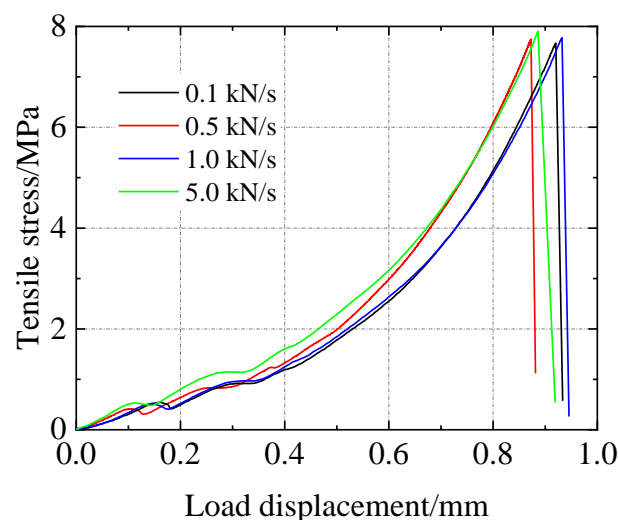


Figure 4. Mechanical response characteristics of specimens under different loading rates.

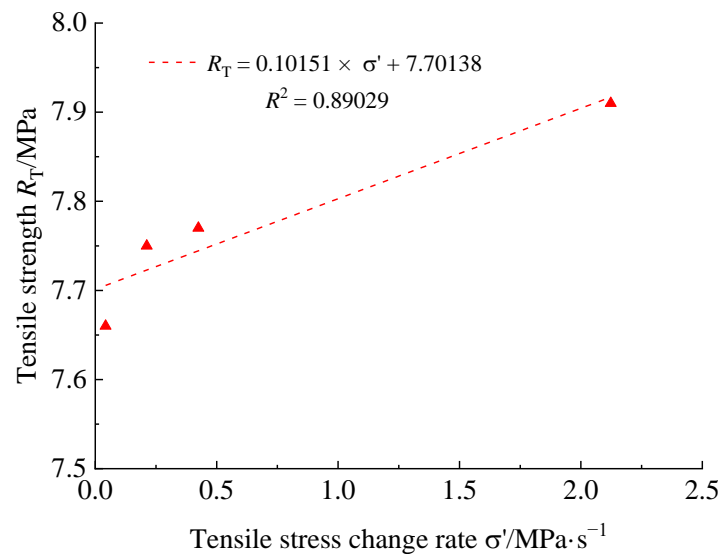


Figure 5. The fitting relationship between tensile strength and tensile stress change rate.

3.2. Spatiotemporal Evolution Characteristics of Acoustic Emission Parameters

Under different loading rate conditions, the variation curves of acoustic emission ring-down counts over time for samples were plotted based on the acoustic emission data obtained from the experiment, aiming to analyze the evolution characteristics of acoustic emission ring-down counts of samples. Due to the significant difference in the order of magnitude of acoustic emission ring-down counts before and at the moment of sample failure, the analysis was divided into two stages for precise examination, as shown in Figure 6.

Figure 6a,b reveal that at a 0.1 kN/s loading rate, acoustic emission counts are mostly under 100, evenly distributed until a surge to 352 just before failure and peaking at 7023 counts at failure, averaging 443 counts/s. According to Figure 6c,d, at a loading rate of 0.5 kN/s, before the peak load, the acoustic emission ring-down counts during the loading process show a slow increasing trend over time, mostly below 200 counts, with a higher value of 886 counts appearing close to sample failure, and the highest value of 10,839 counts at the moment of failure, followed by several weaker ring-down counts, with an overall average level of approximately 3259 counts/s. According to Figure 6e,f, at a loading rate of 1.0 kN/s, before the peak load, the acoustic emission ring-down counts during the loading process exhibit a rapid increasing trend over time, generally below 400 counts, with a higher value of 502 counts appearing close to sample failure, and two higher values of 15,057 and 16,207 counts at the moment of failure, followed by fewer ring-down counts, with an overall average level of approximately 9336 counts/s. According to Figure 6g,h, at a loading rate of 5.0 kN/s, before the peak load, the acoustic emission ring-down counts during the loading process exhibit an exponential rapid increasing trend over time, with ring-down counts mainly concentrated just before sample failure and with high values, reaching up to 1547 counts, with several higher values appearing at the moment of failure, up to 13,718 counts, followed by several weaker ring-down counts, with an overall average level of approximately 15,046 counts/s.

To analyze the evolution characteristics of the acoustic emission energy of samples under different loading rate conditions, variation curves of acoustic emission energy over time for samples under different loading rates were plotted based on the acoustic emission data. Given the significant difference in the magnitude of acoustic emission energy before and at the moment of sample failure, the analysis was also divided into two stages for precise examination, as shown in Figure 7.

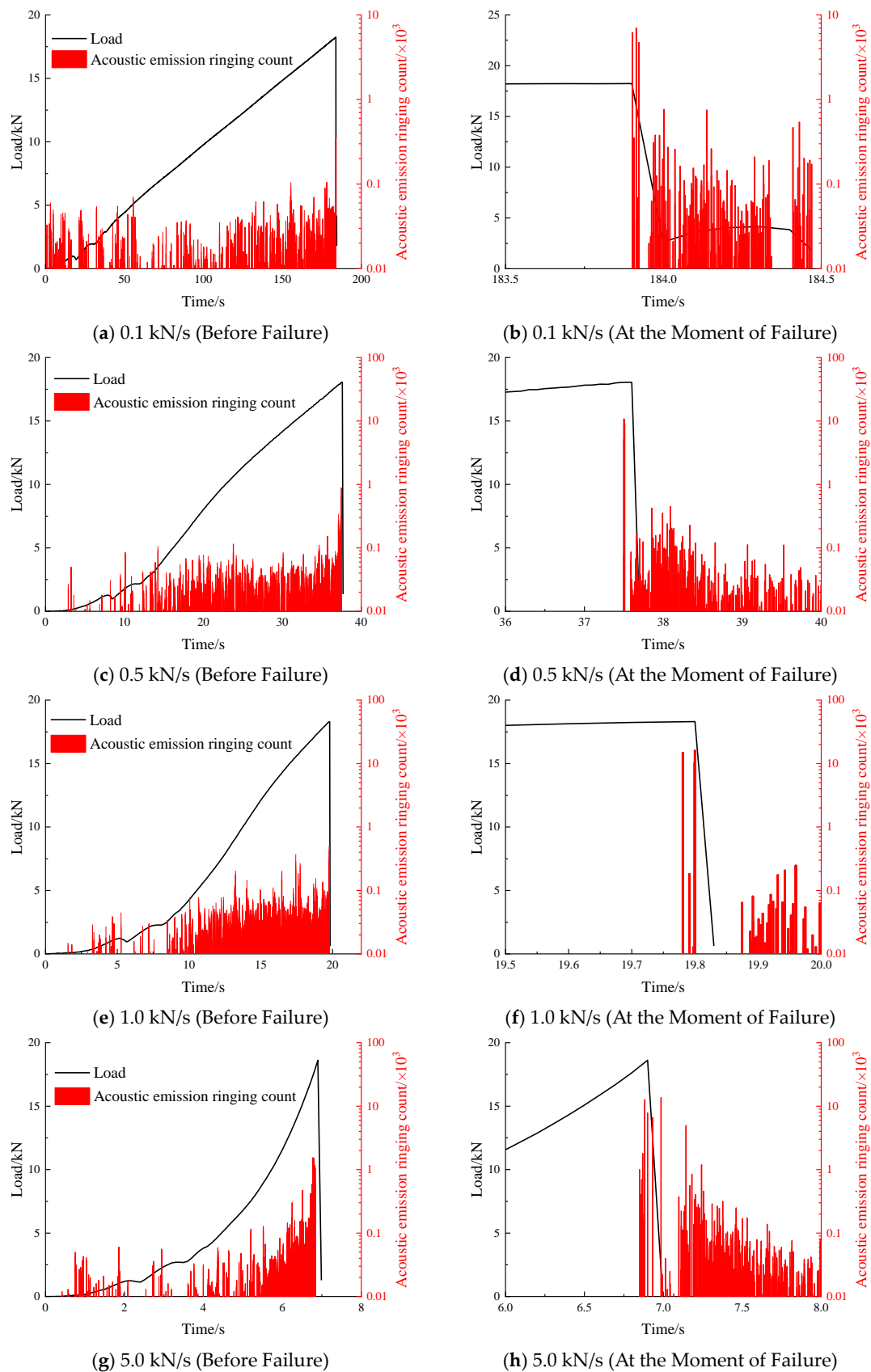


Figure 6. Evolution characteristics of acoustic emission ringing count under different loading rates.

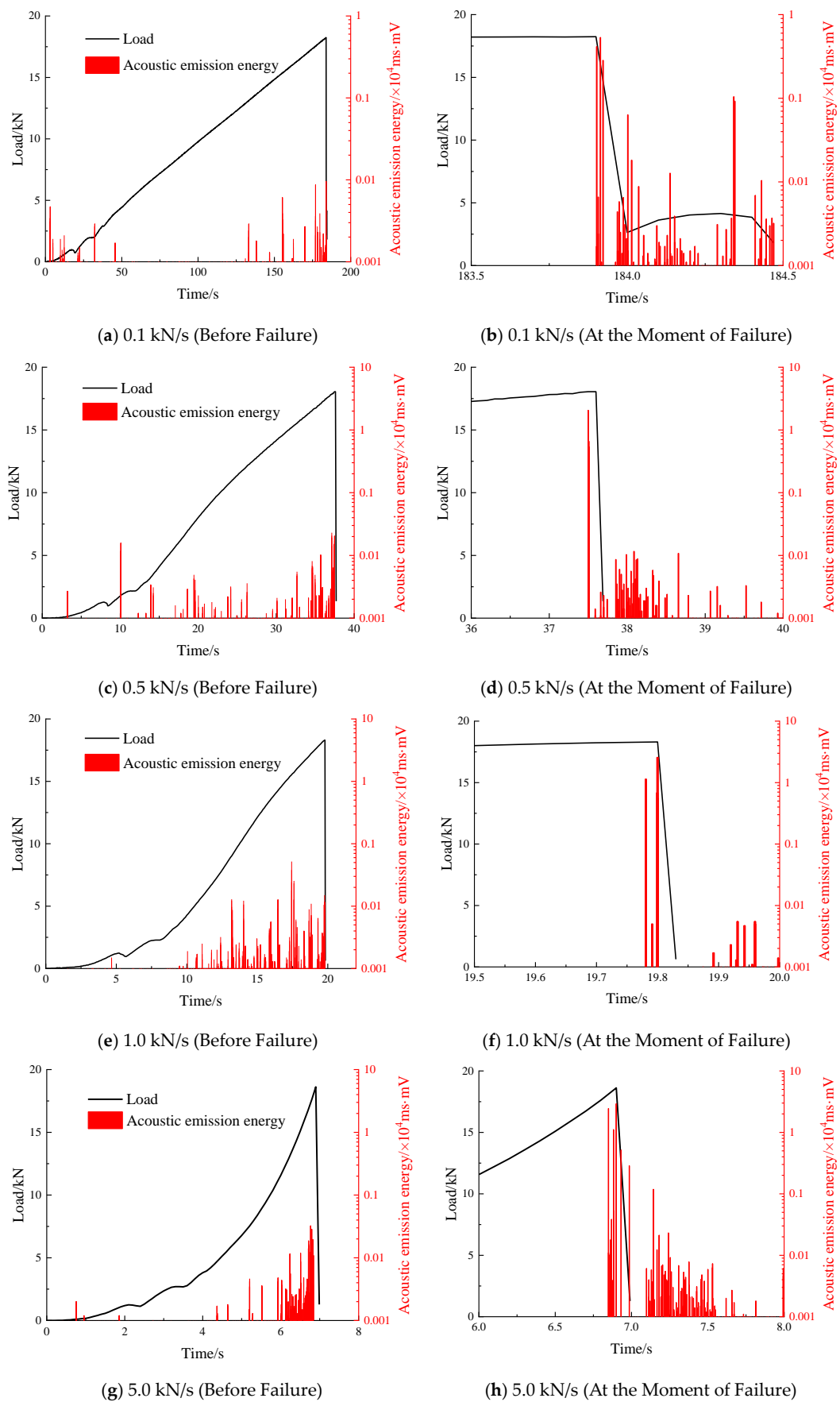
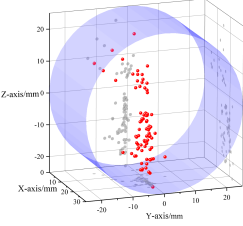
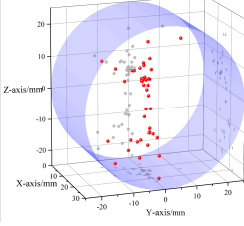
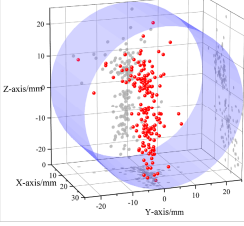

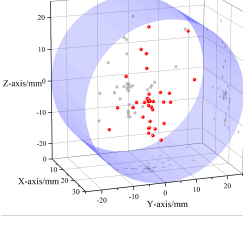
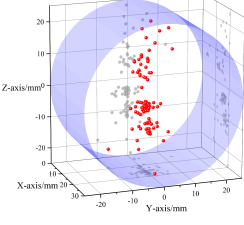
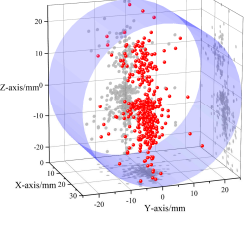

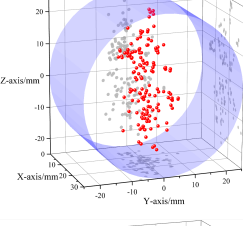
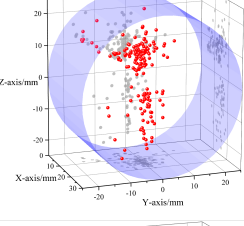
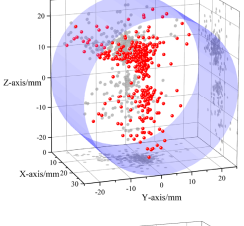

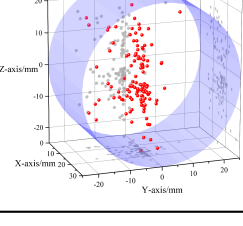
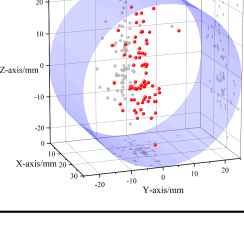
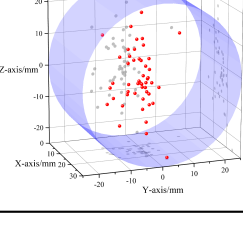



Figure 7. Evolution characteristics of acoustic emission energy under different loading rates.

Figure 7a,b indicate that at a 0.1 kN/s loading rate, acoustic emission energy remains low, under 100 ms·mV, before peaking at 5333 ms·mV upon failure, averaging 122 ms·mV/s. In Figure 7c,d, with a 0.5 kN/s rate, energy ranges up to 250 ms·mV before reaching a maximum of 20,533 ms·mV at failure, with an average of 1224 ms·mV/s. Figure 7e,f show that at 1.0 kN/s, energy levels are below 300 ms·mV until spiking to 25,808 ms·mV at failure, averaging 3493 ms·mV/s. Lastly, Figure 7g,h at 5.0 kN/s show energy levels up to 350 ms·mV before a peak of 29,242 ms·mV at failure, with an average of 9166 ms·mV/s, illustrating a significant increase in acoustic emission energy as loading rates rise.

To analyze the spatial evolution characteristics of acoustic emission (AE) events under different loading rate conditions, spatial distribution maps of AE events during the loading process of samples under different conditions were plotted based on the original AE data obtained from the experiment, as shown in Table 2 (red dots represent the spatial localization of AE events, and gray dots represent the vertical projection on each coordinate plane). The proportion of AE events in different phases under different loading rate conditions is illustrated in Figure 8.

Table 2. Acoustic emission event location and failure state of samples under different loading rates.

Loading Displacement/mm	0~0.4 (Phase I)	0.4~0.7 (Phase II)	>0.7 (Phase III)	Failure State
Loading rate 0.1 kN/s				
Loading rate 0.5 kN/s				
Loading rate 1.0 kN/s				
Loading rate 5.0 kN/s				

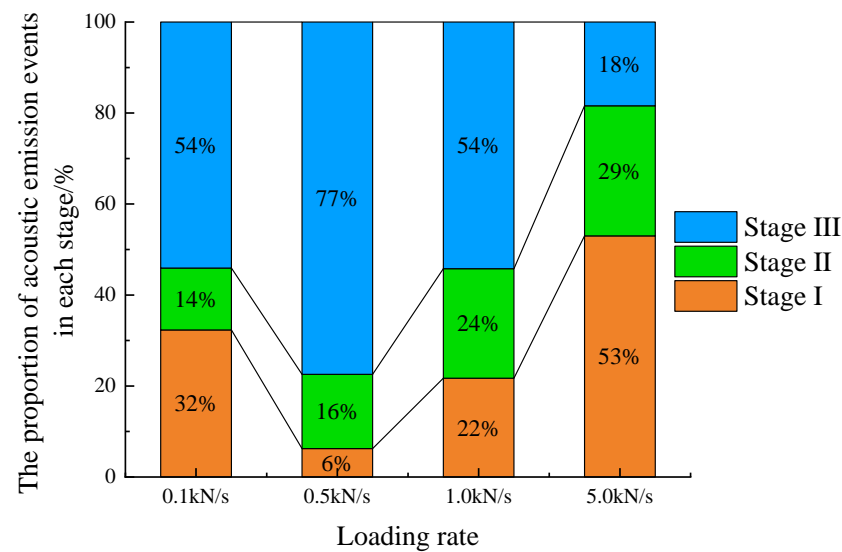


Figure 8. Proportion of acoustic emission events in each stage under different loading rates.

According to Table 2 and Figure 8, at a loading rate of 0.1 kN/s, a total of 331 AE events were located throughout the loading process until sample failure. In phases I and II, fewer AE events were generated, with 107 and 45 events located, accounting for 32% and 14% of the total, respectively. In phase III, a larger number of AE events were observed, with a total of 179 events located, representing 54% of the total. At a loading rate of 0.5 kN/s, a total of 607 AE events were located, with 38 and 99 events located in phases I and II, accounting for 6% and 16% of the total quantity, respectively. In phase III, the number of AE events increased rapidly, with a total of 470 events located, accounting for 77% of the total. At a loading rate of 1.0 kN/s, a total of 769 AE events were located, with 167 and 185 events located in phases I and II, accounting for 22% and 24% of the total, respectively. In phase III, 417 AE events were located, representing 54% of the total. At a loading rate of 5.0 kN/s, a total of 266 AE events were located, with 141 and 76 events located in phases I and II, accounting for 53% and 29% of the total, respectively. In phase III, 49 AE events were located, accounting for 18% of the total.

4. Discussion

4.1. Energy Calculation Model for Hard Roof Considering Mining Speed and Analysis of Influencing Factors

In calculating the initial collapse step distance and cyclic collapse step distance of the roof, two commonly used models are the beam fracture model and the plate fracture model [26]. Generally, both the initial and cyclic collapse step distances of the roof are relatively small compared to the length of the working face. Therefore, a rock beam of unit width (1 m) can be taken from the middle of the working face, and the plane strain theory can be applied to analyze the stress on the roof.

(1) During the Initial Fracture Period

Based on the relevant theories of material mechanics, a beam model for the roof during the initial fracture period is established (as shown in Figure 9). The normal stress (σ) at any point A within the beam is:

$$\sigma = My / J_z \quad (2)$$

where M is the bending moment at the cross-section where the point is located, y is the distance of the point from the neutral axis of the cross-section, and J_z is the moment of inertia about the neutral axis.

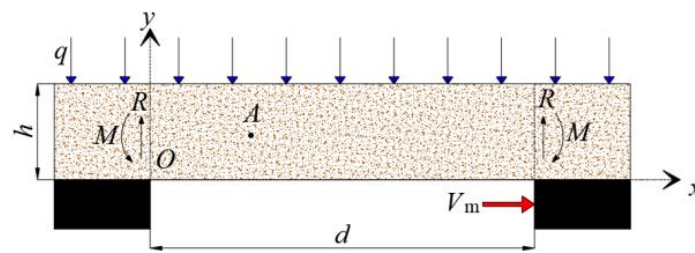


Figure 9. Stress analysis model of roof during initial fracture.

Since the width of the beam is considered to be of unit width, the moment of inertia of the beam section occurs at the point where $J_z = h^3/12$ (where h is the thickness of a single layer of the rock stratum). Therefore, the normal stress σ at any point A can be expressed as $\sigma = 12My/h^3$. Assuming that solid coal exists on both sides before the initial fracture of the roof and that the rock beam is embedded between the overlying rock stratum and the coal seam, it is therefore treated as a fixed support beam for calculation and analysis. The maximum bending moment forms at the ends of the beam, $M_{\max} = -qd^2/12$. Accordingly, the maximum tensile stress at that location is:

$$\sigma_{\max} = \frac{12 \times \frac{1}{12} qd^2 \times \frac{h}{2}}{h^3} = \frac{qd^2}{2h^2} \quad (3)$$

We have taken the mining speed and mining duration in the model to be V_m and t_m , respectively, while in actual production scenarios the face mining speed, mining duration and face length are V_p , t_p , and L , respectively. Assuming that the shearer maintains a uniform speed while cutting back and forth before the initial fracture, and the working face advances at a constant speed, then the span of the rock beam before the initial fracture in the model can be represented as $d = V_m t_m$. In actual production scenarios, $d = V_p t_p$, leading to $V_m t_m = V_p t_p$. Therefore, the mining speed in the model is:

$$V_m = \frac{t_p}{t_m} V_p \quad (4)$$

Let the coefficient $\beta = t_p/t_m$. Since the width of the rock beam in the model is a unit width of 1 m, and the working face length is L , the time spent cutting coal within the unit width of the rock beam accounts for $1/L$ of the entire working face range. Therefore, $\beta = L$, and based on actual conditions, β is taken to be 194.

Substituting the above relationship into Equation (3), the maximum tensile stress in the rock beam can be expressed as:

$$\sigma_{\max} = \frac{q(V_m t_m)^2}{2h^2} = \frac{q(\beta V_p t_m)^2}{2h^2} \quad (5)$$

To find the partial derivative of σ_{\max} with respect to time t_m , we can derive:

$$\dot{\sigma}_{\max} = \frac{\partial \sigma_{\max}}{\partial t_m} = \frac{\partial \sigma_{\max}}{\partial d} \frac{\partial d}{\partial t_m} = \frac{\beta q d}{h^2} V_p \quad (6)$$

Equation (6) shows a linear positive correlation between the change rate of maximum tensile stress in the hard roof and mining speed, indicating that under a specific roof span, a higher mining speed results in a greater change rate of maximum tensile stress.

Research indicates that the tensile strength of coal series sandstone and the change rate of tensile stress approximately exhibit a linear relationship [27]:

$$R_T = a \dot{\sigma} + b \quad (7)$$

where $\dot{\sigma}$ represents the change rate of tensile stress, a and b are constants related to the rock type, which, based on previous laboratory results, are taken to be 0.10151 and 7.70138, respectively.

Based on Equations (6) and (7), the tensile strength can be expressed as:

$$R_T = \frac{a\beta q d}{h^2} V_p + b \quad (8)$$

Based on knowledge from material mechanics, the maximum span of a rock beam with fixed supports at both ends at the time of initial fracture is given by $d_{\max} = h (2R_T/q)^{1/2}$. By combining Equation (8) to eliminate R_T and then rearranging, we can obtain a quadratic equation in terms of d_{\max} :

$$d_{\max}^2 - 2a\beta V_p d_{\max} - \frac{2bh^2}{q} = 0 \quad (9)$$

To find the real roots of this equation, we first calculate the discriminant Δ and find that $\Delta > 0$, indicating that the equation has two distinct real roots. Solving the equation, we can obtain the two real roots as follows:

$$d_{\max} = \begin{cases} a\beta V_p + \sqrt{a^2\beta^2 V_p^2 + \frac{2bh^2}{q}} \\ \text{or} \\ a\beta V_p - \sqrt{a^2\beta^2 V_p^2 + \frac{2bh^2}{q}} \end{cases} \quad (10)$$

Clearly, the second root being negative is not practically meaningful, so we analyze the first root with a positive sign. According to Prof. Avilsen's viewpoint, the elastic energy of the coal-rock layer system primarily consists of the volumetric elastic energy of the coal (U_V), the deformation elastic energy of the coal (U_t), and the bending elastic energy of the roof (U_w) [26]. The bending elastic energy of the roof at the time of initial fracture is:

$$U_w = \frac{q^2 d^5}{576 E J_z} \quad (11)$$

By substituting the positive root from Equation (10) into Equation (11), and incorporating the values of the coefficients a , b , and β , we can derive an equation as follows:

$$U_w = \frac{q^2}{48 E h^3} \left(19.4 \cdot V_p + \sqrt{376.36 \cdot V_p^2 + \frac{15.4 \cdot h^2}{q}} \right)^5 \quad (12)$$

which describes the relationship between the accumulated bending elastic energy at the limit span during the initial fracture process of the roof and the mining speed of the working face.

(2) During Cyclic Fracture

Assuming that the roof fractures in the form of a cantilever beam during cyclic fracture processes (as shown in Figure 10), then the maximum tensile stress within the rock beam at the point of maximum bending moment $M_{\max} = qd^2/2$ is:

$$\sigma_{\max} = \frac{12 \times \frac{qd^2}{2} \times \frac{h}{2}}{h^3} = \frac{3qd^2}{h^2} \quad (13)$$

Using the same method as in Section 4.1, we can derive the relationship between the accumulated bending elastic energy at the limit span during the cyclic fracture process of the roof and the mining speed of the working face:

$$U'_w = \frac{3q^2}{2Eh^3} \left(19.4 \cdot V_p + \sqrt{376.36 \cdot V_p^2 + \frac{2.6 \cdot h^2}{q}} \right)^5 \quad (14)$$

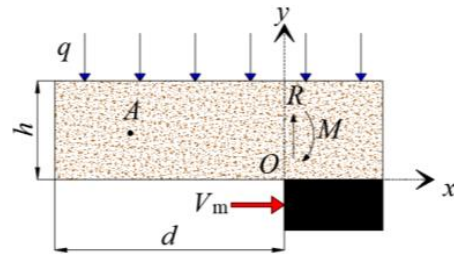


Figure 10. Stress analysis model of roof during periodic fracture.

(3) Analysis of Influencing Factors

To investigate the influence of the elastic modulus and thickness of hard roofs on the relationship between bending elastic energy and mining speed, a single-factor analysis method was utilized. The variation curves of bending elastic energy with mining speed under different influencing factors were drawn, as shown in Figures 11 and 12, respectively. It is observed that the bending elastic energy approximately exhibits linear growth with the increase in mining speed. Under the same conditions of mining speed, elastic modulus, and thickness, the bending elastic energy during the initial fracture period of the hard roof is higher than that during cyclic fractures, indicating that the elastic energy released during the initial fracture of the hard roof is higher than that during cyclic fractures.

According to Figure 11, the smaller the elastic modulus of the hard roof, the greater the accumulated bending elastic energy, and the stronger the sensitivity of the bending elastic energy to changes in mining speed. This sensitivity difference is more pronounced during cyclic fracture periods. For instance, during the initial fracture period, with an elastic modulus of 30 GPa, as the mining speed increases from 0.6 m/d to 6.0 m/d, the bending elastic energy increases from 198 kJ to 210 kJ, with a growth of 12 kJ; with an elastic modulus of 5 GPa, as the mining speed increases from 0.6 m/d to 6.0 m/d, the bending elastic energy increases from 1189 kJ to 1260 kJ, with a growth of 71 kJ. By comparison, during the cyclic fracture period, with an elastic modulus of 30 GPa, as the mining speed increases from 0.6 m/d to 6.0 m/d, the bending elastic energy increases from 169 kJ to 194 kJ, with a growth of 25 kJ; with an elastic modulus of 5 GPa, as the mining speed increases from 0.6 m/d to 6.0 m/d, the bending elastic energy increases from 1012 kJ to 1166 kJ, with a growth of 154 kJ.

According to Figure 12, the thicker the hard roof, the larger the accumulated bending elastic energy, and the stronger the sensitivity of the bending elastic energy to changes in mining speed. This sensitivity difference is more pronounced during cyclic fracture periods. For instance, with a 10 m thickness, increasing the mining speed from 0.6 m/d to 6.0 m/d raises the bending elastic energy from 38 kJ to 48 kJ, a 10 kJ increase. At 60 m thickness, this speed increase boosts the energy from 1334 kJ to 1387 kJ, a 53 kJ growth. By comparison, during the cyclic fracture period, for a thickness of 10 m, as the mining speed increases from 0.6 m/d to 6.0 m/d, the bending elastic energy increases from 33 kJ to 58 kJ, with a growth of 25 kJ; for a thickness of 60 m, as the mining speed increases from 0.6 m/d to 6.0 m/d, the bending elastic energy increases from 1132 kJ to 1245 kJ, with a growth of 113 kJ.

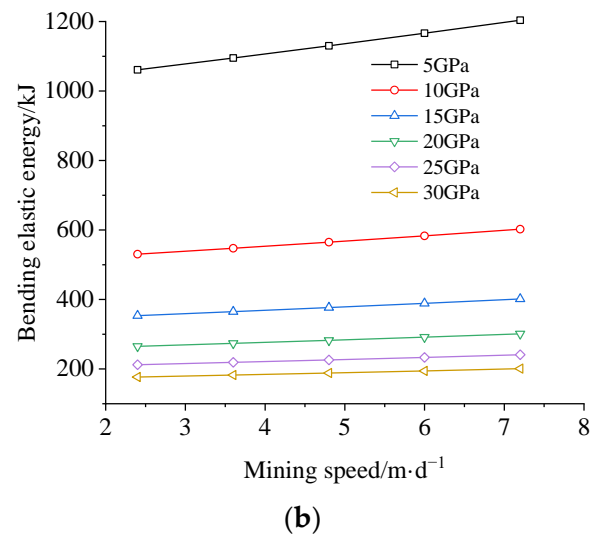
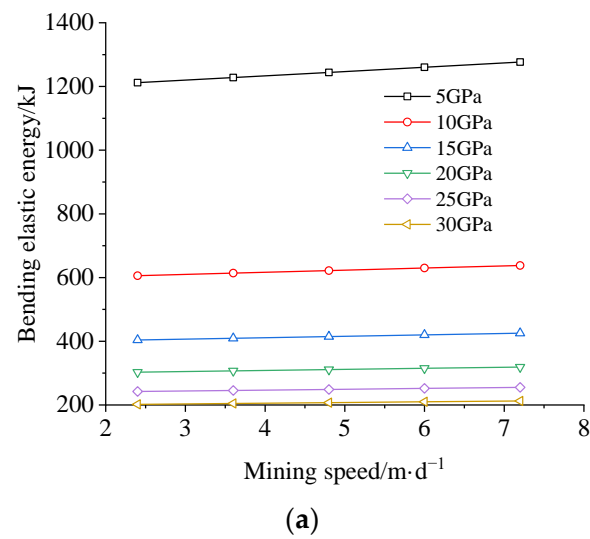


Figure 11. Variation in bending elastic energy of hard roof with mining speed under different elastic modulus. (a) During Initial Fracture, (b) During Cyclic Fracture.

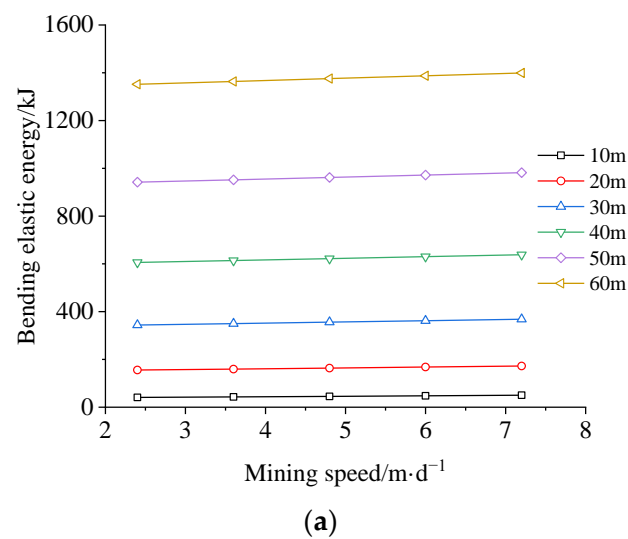


Figure 12. Cont.

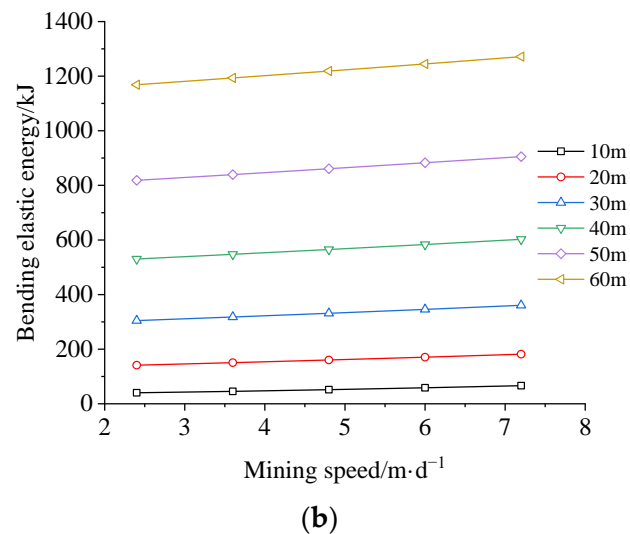


Figure 12. Variation in bending elastic energy of hard roof with mining speed under different thickness. (a) During Initial Fracture, (b) During Cyclic Fracture.

4.2. Future Works

In sandstone Brazilian split test samples, the range of acoustic emission energy distribution widens with increasing loading rates before failure. Additionally, both the acoustic emission ring-down counts and the energy experience a substantial increase at the point of failure. At lower loading rates, the generation of acoustic emission events mainly concentrates in Stage III near sample failure, while at higher loading rates, the generation of acoustic emission events primarily occurs in the early loading phase (Stages I and II). These differences in acoustic emission parameter characteristics indicate that the higher the mining speed, the less sufficient the development and extension of internal micro-cracks before the hard roof fractures, manifesting macroscopically as an increase in tensile strength and an increase in the amount of energy released at the time of fracture. The analysis of influencing factors of the energy calculation model reveals that the greater the thickness of the hard roof, the higher the sensitivity of the bending elastic energy to changes in mining speed, and this characteristic is more pronounced during cyclic fractures. Therefore, when mining workfaces with thick and hard roofs, the optimization of mining speed should be emphasized to prevent the occurrence of rockbursts.

This study focuses on the hard roof of coal seams to mitigate roof fracture-induced rockbursts. It examines the tensile failure properties of hard roofs in relation to mining speed and formulates a model for calculating the bending elastic energy of hard roofs, considering the influence of mining speed. These insights are crucial for understanding how mining speed affects the risk of roof fracture-type rockbursts. Nonetheless, in the context of rockbursts, coal itself is primarily prone to failure and outburst, with the loading rate significantly affecting the coal's mechanical characteristics [28–32]. Future research will aim to link mining speed with the risk of coal face outbursts, building on this paper's findings.

5. Conclusions

- (1) The tensile strength and pre-peak energy accumulation of sandstone Brazilian split test samples gradually increase with the increase in loading rate. The coefficients a and b in the linear relationship between tensile strength and the change rate of tensile stress are 0.10151 and 7.70138, respectively. As mining speed increases, internal micro-cracks in the hard roof have less time to develop and expand before fracturing. This results in a macroscopic increase in tensile strength and a higher amount of energy released upon fracture.
- (2) The maximum rate of change of tensile stress in the hard roof during initial and cyclic fractures shows a linear positive correlation with the mining speed. The bending

elastic energy approximately exhibits linear growth with the increase in mining speed. Under the same conditions of mining speed, elastic modulus, and thickness, the bending elastic energy during the initial fracture of the hard roof is higher than that during cyclic fractures.

- (3) Through theoretical deduction, the relationship between the mining speed and the change rate of tensile stress within the hard roof was obtained. A computational model for the bending elastic energy of the hard roof during initial and cyclic fracture periods, considering the mining speed, was established, and an analysis of the main influencing factors was conducted.
- (4) The thicker the hard roof, the higher the sensitivity of the bending elastic energy to changes in mining speed, and this characteristic is more pronounced during cyclic fractures. Therefore, when mining workfaces with thick and hard roofs, the optimization of mining speed should be emphasized to effectively prevent roof fracture-type rockburst.

Author Contributions: Methodology, W.L.; Project administration, S.T. and T.Z. All authors have read and agreed to the published version of the manuscript.

Funding: This research was funded by the National Natural Science Foundation of China (51874281) and the China National Natural Science Foundation Youth Funding Project (52004270).

Institutional Review Board Statement: Not Applicable.

Informed Consent Statement: Not Applicable.

Data Availability Statement: The data presented in this study are available in the article.

Conflicts of Interest: The authors declare no conflict of interest.

References

- Qi, Q.X.; Pan, Y.S.; Li, H.T.; Jiang, D.Y.; Shu, L.Y.; Zhao, S.K.; Zhang, Y.; Pan, J.; Li, H.; Pan, P. Theoretical basis and key technology of prevention and control of coal-rock dynamic disasters in deep coal mining. *J. China Coal Soc.* **2020**, *45*, 18.
- Yang, S.L.; Wang, Z.H.; Jiang, W.; Yang, J.H. Advancing rate effect on rock and coal failure format in highintensity mining face. *J. China Coal Soc.* **2016**, *41*, 586–594.
- Wu, M. The effect of loading rate on the compressive and tensile strength of rocks. *Chin. J. Geotech. Eng.* **1982**, *4*, 97–106.
- Li, H.; Li, J.; Liu, B.; Li, J.; Li, S.; Xia, X. Direct tension test for rock material under different strain rates at quasi-static loads. *Rock Mech. Rock Eng.* **2013**, *46*, 1247–1254. [[CrossRef](#)]
- Zhou, H.; Yang, Y.S.; Xiao, H.B.; Zhang, C.Q.; Fu, Y.P. Research on loading rate effect of tensile strength property of hard brittle marble—Test characteristics and mechanism. *Chin. J. Rock Mech. Eng.* **2013**, *32*, 1868–1875.
- Gong, F.Q.; Zhao, G.F. Dynamic indirect tensile strength of sandstone under different loading rates. *Rock Mech. Rock Eng.* **2014**, *47*, 2271–2278. [[CrossRef](#)]
- Yang, J.H.; Yu, X. Mechanical explanation of loading rate impact on tensile strength and its numerical simulation analysis. *J. China Coal Soc.* **2017**, *42*, 51–59.
- Deng, H.; Wang, C.; Li, J.; Zhang, Y.; Wang, W.; Zhang, H. Influence mechanism of loading rate on tensile strength of sandstone. *Rock Soil Mech.* **2018**, *39*, 79–88.
- Cui, Z.; Qian, S.; Zhang, G.; Maochu, Z. An experimental investigation of the influence of loading rate on rock tensile strength and split fracture surface morphology. *Rock Mech. Rock Eng.* **2021**, *54*, 1969–1983. [[CrossRef](#)]
- Liu, Y.; Huang, D.; Cen, D.; Zhong, Z.; Gong, F.; Wu, Z.; Yang, Y. Tensile strength and fracture surface morphology of granite under confined direct tension test. *Rock Mech. Rock Eng.* **2021**, *54*, 4755–4769. [[CrossRef](#)]
- Liu, B.; Zhao, Y.; Wang, H.; Gao, Y.; Sun, Z. Tensile properties and multiparameter response characteristics of coal under different loading rates. *Nat. Resour. Res.* **2022**, *31*, 2787–2803. [[CrossRef](#)]
- Vasylyev, L.; Malich, M.G.; Vasylyev, D.; Katan, V.; Rizo, Z. Improving a technique to calculate strength of cylindrical rock samples in terms of uniaxial compression. *Min. Miner. Depos.* **2023**, *17*, 43–50. [[CrossRef](#)]
- Winkler, M.B.; Frühwirt, T.; Marcher, T. Elastic Behavior of Transversely Isotropic Cylindrical Rock Samples under Uniaxial Compression Considering Ideal and Frictional Boundary Conditions. *Appl. Sci.* **2023**, *14*, 17. [[CrossRef](#)]
- Piscopo, V. Ultimate Strength of Platings Under Uniaxial Compression with Edges Elastically Restrained Against Torsion: A New Comprehensive Approach. *J. Mar. Sci. Appl.* **2024**, *23*, 443–459. [[CrossRef](#)]
- Choo, J.; Sun, Y.; Fei, F. Size effects on the strength and cracking behavior of flawed rocks under uniaxial compression: From laboratory scale to field scale. *Acta Geotech.* **2023**, *18*, 3451–3468. [[CrossRef](#)]

16. Tomporowski, D.; Nitka, M.; Tejchman, J. Application of the 3D DEM in the modelling of fractures in pre-flawed marble specimens during uniaxial compression. *Eng. Fract. Mech.* **2023**, *277*, 108978. [[CrossRef](#)]
17. Feng, L.F.; Dou, L.M.; Wang, X.D.; Jin, D.W.; Cai, W.; Xu, G.G.; Jiao, B. Mechanism of mining advance speed on energy release from hard roof movement. *J. China Coal Soc.* **2019**, *44*, 3329–3339.
18. Zhao, T.; Guo, W.; Han, F.; Gu, S. Analysis on energy accumulation and release of roof under influence of mining speed. *Coal Sci. Technol.* **2018**, *46*, 37–44.
19. Peng, S.J.; Chen, C.C.; Xu, J.; Zhang, H.L.; Tang, Y.; Nie, W.; Zhao, K. Loading rate dependency of rock stress-strain curve based on Brazil splitting test. *Chin. J. Rock Mech. Eng.* **2018**, *37*, 3247–3252.
20. Su, H.; Jing, H.; Du, M.; Wang, C. Experimental investigation on tensile strength and its loading rate effect of sandstone after high temperature treatment. *Arab. J. Geosci.* **2016**, *9*, 616. [[CrossRef](#)]
21. Yu, M.; Wei, C.; Niu, L. The Coupled Effect of Loading Rate and Grain Size on Tensile Strength of Sandstones under Dynamic Disturbance. *Shock. Vib.* **2017**, *2017*, 6989043. [[CrossRef](#)]
22. Liu, J.; Jiang, G.; Liu, T.; Liang, Q. The Influence of Loading Rate on Direct and Indirect Tensile Strengths: Laboratory and Numerical Methods. *Shock. Vib.* **2021**, *2021*, 3797243. [[CrossRef](#)]
23. Zhang, M.C.; Sheng, Q.; Cui, Z.; Ma, Y.L.N.; Zhou, G.X. Effect of loading rate on tensile strength of rock materials and morphology of fracture joint surface. *Rock Soil Mech.* **2020**, *41*, 1169–1178.
24. GB/T 23561.10-2010; Methods for Determining the Physical and Mechanical Properties of Coal and Rock Part 10: Methods for Determining the Tensile Strength of Coal and Rock. General Administration of Quality Supervision, Inspection and Quarantine of the People's Republic of China: Beijing, China, 2010.
25. Li, H.T.; Song, L.; Zhou, H.W.; Jiang, Y.D.; Wang, H.W. Evaluation method and application of coal burst performance under the effect of loading rate. *J. China Coal Soc.* **2015**, *40*, 2763–2771.
26. Qian, M.; Shi, P.; Xu, J. *Ground Pressure and Strata Control*; China University of Mining and Technology Press: Xuzhou, China, 2010.
27. Mao, R. Study on Tensile Properties and Damage Evolution Mechanism of Coal Measures Sandstone under High Strain Rate. Ph.D. Thesis, China University of Mining and Technology, Xuzhou, China, 2018.
28. Li, H.T.; Jiang, C.X.; Jiang, Y.D.; Wang, H.W.; Liu, H.B. Mechanical behavior and mechanism analysis of coal samples based on loading rate effect. *J. China Univ. Min. Technol.* **2015**, *44*, 430–436.
29. Li, H.T.; Song, L.; Zhou, H.W.; Song, F. Experimental study of nonlinear evolution mechanism of coal strength under multi-loading rates and its application. *Chin. J. Rock Mech. Eng.* **2016**, *35*, 2978–2989.
30. Li, H.; Zhou, H.; Jiang, Y.; Wang, H. An Evaluation Method for the Bursting Characteristics of Coal Under the Effect of Loading Rate. *Rock Mech. Rock Eng.* **2016**, *49*, 3281–3291.
31. Gao, M.; Xie, J.; Gao, Y.; Wang, W.; Li, C.; Yang, B.; Liu, J.; Xie, H. Mechanical behavior of coal under different mining rates: A case study from laboratory experiments to field testing. *Int. J. Min. Sci. Technol.* **2021**, *31*, 825–841. [[CrossRef](#)]
32. Li, H.; Qi, Q.; Du, W.; Li, X. A criterion of rockburst in coal mines considering the influence of working face mining velocity. *Geomech. Geophys. Geo-Energy Geo-Resour.* **2022**, *8*, 37. [[CrossRef](#)]

Disclaimer/Publisher's Note: The statements, opinions and data contained in all publications are solely those of the individual author(s) and contributor(s) and not of MDPI and/or the editor(s). MDPI and/or the editor(s) disclaim responsibility for any injury to people or property resulting from any ideas, methods, instructions or products referred to in the content.